Journal of Sound and Vibration 330 (2011) 526–544

Contents lists available at ScienceDirect

Journal of Sound and Vibration

journal homepage: www.elsevier.com/locate/jsvi

New breathing functions for the transverse breathing crack of the cracked rotor system: Approach for critical and subcritical harmonic analysis

Mohammad A. Al-Shudeifat *, Eric A. Butcher

Department of Mechanical and Aerospace Engineering, New Mexico State University, P.O. Box 30001, MSC 3450, Las Cruces, NM 88003, USA

ARTICLE INFO

Article history:
Received 10 December 2009
Received in revised form
12 August 2010
Accepted 12 August 2010
Handling Editor: H. Ouyang
Available online 9 September 2010

ABSTRACT

The actual breathing mechanism of the transverse breathing crack in the cracked rotor system that appears due to the shaft weight is addressed here. As a result, the correct time-varying area moments of inertia for the cracked element cross-section during shaft rotation are also determined. Hence, two new breathing functions are identified to represent the actual breathing effect on the cracked element stiffness matrix. The new breathing functions are used in formulating the time-varying finite element stiffness matrix of the cracked element. The finite element equations of motion are then formulated for the cracked rotor system and solved via harmonic balance method for response, whirl orbits and the shift in the critical and subcritical speeds. The analytical results of this approach are compared with some previously published results obtained using approximate formulas for the breathing mechanism. The comparison shows that the previously used breathing function is a weak model for the breathing mechanism in the cracked rotor even for small crack depths. The new breathing functions give more accurate results for the dynamic behavior of the cracked rotor system for a wide range of the crack depths. The current approach is found to be efficient for crack detection since the critical and subcritical shaft speeds, the unique vibration signature in the neighborhood of the subcritical speeds and the sensitivity to the unbalance force direction all together can be utilized to detect the breathing crack before further damage occurs.

1. Introduction

Rotordynamic systems have had many applications for many decades. Gas turbines and compressors are examples of heavy rotating machines that are driven by rotating shafts which are intensively used in power generation field and aircrafts. In addition, most of the heavy industries have a basic use of rotating machines. The extensive use of these rotordynamic systems with continuous heavy loading may yield an unpredicted failure and damage that leads to a loss in life and equipments. These damages almost always occur due to propagating fatigue cracks that lead to sudden and destructive vibration scenarios. The breathing fatigue crack has a great deal of attention in literature as one of the main causes of these dangerous damages in rotor systems. The breathing mechanism of the crack that appears in rotating machinery is mainly due to the shaft weight. Several studies have focused on two models of fatigue cracks that are affected

---

* Corresponding author. Tel.: +1 575 646 3501; fax: +1 575 646 6111.
E-mail addresses: shdefat@nmsu.edu, shdefat@aol.com (M.A. Al-Shudeifat).

doi:10.1016/j.jsv.2010.08.022

Nomenclature

A_1	the left uncracked area at $\theta=0$
A_2	area of the closed portion of the crack
A_c	area of the crack segment at $\theta=0$ (fully open crack)
A_{ce}	overall cracked element cross-sectional area
ce	centroid of the cross-section
E	elastic modulus
e	centroid location of A_1 in Y-axis
h	crack depth in the radial direction
I	area moment of inertia of a circular section
I_1	area moment of inertia of the uncracked segment (A_1) about X-axis
I_2	area moment of inertia of the uncracked segment (A_1) about Y-axis
I_X	area moment of inertia of the overall cross-sectional area of the cracked element (A_{ce}) about X-axis
I_Y	area moment of inertia of the overall cross-sectional area of the cracked element (A_{ce}) about Y-axis
$\hat{I}_X$	time-periodic approximate formula for the exact I_X
$\hat{I}_Y$	time-periodic approximate formula for the exact I_Y
$I_X^{A_1}$	area moment of inertia of the uncracked segment (A_1) about X-axis
$I_Y^{A_1}$	area moment of inertia of the uncracked segment (A_1) about Y-axis
$I_X^{A_2}$	area moment of inertia of the closed portion of the crack (A_2) about X-axis
$I_Y^{A_2}$	area moment of inertia of the closed portion of the crack (A_2) about Y-axis
I_x^c	area moment of inertia of the crack segment (A_c) about X-axis
I_y^c	area moment of inertia of the crack segment (A_c) about Y-axis
L	length of the shaft
l	length of the element in the finite element model
N.A.	neutral axis
O	origin of the fixed coordinate system
R	shaft radius
X, Y	fixed coordinate system
$\overline{X}$,$\overline{Y}$	fixed centroidal axes of the cracked element cross-section
x, y	rotating-coordinate system
$\overline{x}$,$\overline{y}$	rotating centroidal axes
X_{ce}	the centroid coordinates of the cracked element cross-sectional area in X-axis
X_i	the centroid coordinates in X-axis for the area A_i for $i=1, \ldots, 4$
Y_{ce}	the centroid coordinates of the cracked element cross-sectional area in Y-axis
Y_i	the centroid coordinates in Y-axis for the area A_i for $i=1, \ldots, 4$
μ	crack depth ratio
θ	angle of rotation
Ω	rotational speed of the rotor
ω_{bi}	the ith critical backward whirl speed
ω_{fi}	the ith critical forward whirl speed

by the static deflection of the rotor, namely the switching and breathing crack models. Finding an efficient model of the breathing crack in rotor systems may help in identifying a unique vibration signature of the cracked rotor that assists in the early detection of the crack before damage occurs due to further crack propagation.

Different techniques have been used in the literature for modeling the transverse crack in rotating shafts. The flexibility matrix method has been utilized for modeling the stiffness of the cracked rotor with breathing crack [1–6]. The coupling of the longitudinal and bending vibration in a cracked shaft was studied for the system with an open transverse crack in Ref. [1] and two transverse breathing cracks in Ref. [2] in which the breathing mechanism was found to depend on the direction of the excitation load. It was found that there are variations in the critical frequencies as the crack depth increases for the open crack case. The analytical and the experimental results have verified the effect of the coupling on both transverse vibration directions for the breathing crack case. The finite element method (FEM) was used in modeling the equations of motion of the cracked rotor in Refs. [3–6] where the flexibility matrix was also used in modeling the stiffness matrix of the cracked element.

The finite element stiffness matrix of a rod in space found in Ref. [7] was used to represent the cracked element stiffness matrix in Refs. [8–12] where the time-varying element stiffness matrix of the cracked element was considered. The classical breathing function proposed in Ref. [13] was used to express the time change in the stiffness of the cracked element during rotation. This results in a time-varying element stiffness matrix due to the breathing mechanism of the crack. The finite element equations of motion were solved using the harmonic balance (HB) method. The shapes of the orbits in the neighborhood of subcritical speeds and the emerged resonance peaks at these speeds can be used for crack detection in rotor systems. In addition, the shift in the critical and subcritical speeds as a function of the crack size was verified in Ref. [12] via waterfall plots.

The behavior of the cracked rotor in the neighborhood of the subcritical speeds was also studied in Refs. [14–22]. The transfer matrix method was employed in studying the behavior of the cracked rotor system where the second harmonic characteristics are used in detecting the crack in the system [14]. In addition, the transfer matrix method was utilized to find the cracked rotor response of a simple rotor model in Ref. [15]. It was noticed that there is a temporary whirl reversal and phase shift near to the critical and subcritical speeds due to instability in the neighborhood of these speeds.

The nonlinear behavior of the cracked rotor was studied in Ref. [16] where new peaks of vibration have appeared at half and one third of the critical speeds. A theoretical cracked beam model was used for detecting cracks in power plant rotating machines [17]. The vibration amplitudes in the neighborhood of the first subcritical speed (1/2 first critical speed) were used in detecting the crack while a good match was found between the numerical and experimental results. The nonlinear dynamic behavior of the cracked Jeffcott rotor with switching and breathing crack models was also studied in Ref. [18]. Chaos and bifurcation were observed only in the case of a switching crack. An experimental analysis of a cracked rotor in the neighborhood of the subcritical speeds was performed in Ref. [19]. The effects of the crack depth and the additional eccentricity were verified experimentally via the shapes of the orbits, response and waterfall plots for the shaft with an open crack. The cracked rotor response during the passage through subcritical speeds was discussed in Refs. [20,21] where the two loops orbit appears in the neighborhood of the 1/2 the critical speed. This behavior of the orbit before and after the critical speed can be utilized as an indication of a propagating crack in the rotor system.

A review of the strain energy release rate approach (SERR) for different modeling techniques of open, switching and breathing cracks and their corresponding methods of solution was introduced in Ref. [22]. Some of these modeling techniques have already been overviewed in this introduction.

Most of the above techniques have considered some assumptions in modeling the breathing crack. Hence, the breathing mechanism of the breathing crack was almost an approximation of the actual breathing of the crack. In this study, the actual breathing mechanism is presented and new breathing functions of the breathing crack are introduced. The correct time-varying stiffness matrix is formulated and incorporated to the global stiffness matrix in the finite element model of the cracked rotor with breathing crack. The harmonic balance method is employed for finding the response, orbits and critical and subcritical speeds of a cracked rotor system. The analytical results of this approach are compared with some published results in which other techniques or forms for breathing mechanism were used. It is found that some of the previous studies have used an approximate formula of the breathing function [8–13,23]. It is shown that the new breathing functions introduced in this study are considerably more accurate than the previously used functions in the literature. It is found that for small breathing crack depths, high vibration amplitudes with unique whirl orbits appear during the passage through the subcritical speeds. These amplitudes of vibration that appear for these small crack depths were barely observable when the old breathing function was used. The unique whirl orbits that appear for small breathing crack depths in the neighborhoods of subcritical speeds can be used as an early indication of breathing crack propagation.

2. Actual breathing mechanism of the breathing crack model

An approach for calculating the accurate breathing mechanism of the crack in a cracked rotor was introduced in Ref. [24]. In this approach a linear stress/strain distribution was assumed in the crack location to approximate the actual breathing of the crack found via three-dimensional nonlinear finite element calculations. An excellent agreement has been found between the simplified linear model and the nonlinear finite element model for finding the accurate breathing mechanism of the crack. Even though highly accurate breathing calculations have been performed, no mathematical formulas of the breathing mechanism were introduced. It is necessary to introduce breathing functions that closely approximate the actual breathing mechanism of the crack where the time-varying stiffness matrix can be formulated and incorporated to the linear time-periodic equations of motion of the cracked rotor system. The aim here in this paper is to find these actual time-periodic breathing functions which can be used in formulating the time-varying stiffness matrix in the finite element equations of motion of the cracked rotor. These equations of motion are solvable via the harmonic balance method. The breathing mechanism occurs in the cracked rotor when the vibration is dominated by the static deflection of the shaft and the transverse thickness of the crack in the axial direction is very small. If the shaft length and diameter are large enough, the neutral axis almost passes through the centroid of the cracked element cross-sectional area.

In addition, the torsional and longitudinal vibrations are assumed to be dominated by the transverse bending vibration in the proposed model of this study especially in large turbine–generator shafts where the longitudinal vibration is restrained (minimized) by the effect of the use of many journal and thrust bearings. In such large machines, the weight of the rotor overcomes the dynamic loads where the static deflections dominate the vibration. However, in the vertical shafts the static deflection is dominated by the dynamic vibration amplitude which results in a nonlinear cracked rotor system [22]. As the shaft starts to rotate, the locations of the centroid and the neutral axis of the cracked element are changed with time during rotation as shown in Fig. 1. The tension stress field exists below the neutral axis which tends to keep the crack open. The compression stress field that exists above the neutral axis tends to compress the crack to be closed as shown in the figure.

The crack is modeled as shown in Fig. 2 where the dashed segment represents the crack segment. The edge of the crack is assumed at zero angle with the fixed X-axis at $t=0$ as shown in Fig. 2a. As the shaft starts to rotate, the crack angle with the negative Y-axis is changed by time to Ωt as shown in Fig. 2b.

The cross-sectional area of the cracked element at $t=0$ and the centroid location e on the fixed Y-axis are given as

$$A_1 = R^2(\pi - \cos^{-1}(1-\mu) + (1-\mu)\gamma) \tag{1a}$$

$$e = \frac{2R^3}{3A_1}(\mu(2-\mu))^{3/2} = \frac{2R^3}{3A_1}\gamma^3 \tag{1b}$$

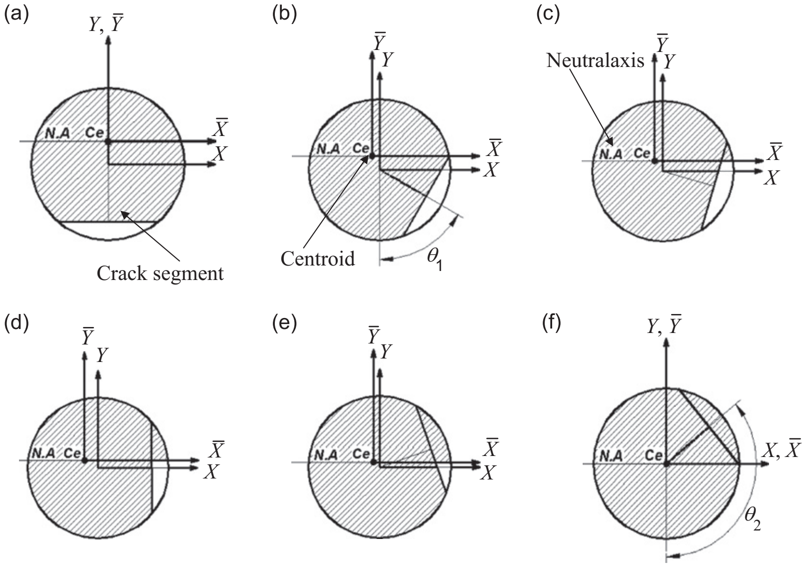

Fig. 1. States of the breathing crack and centroid locations of the cracked element cross-section for different angles of rotation.

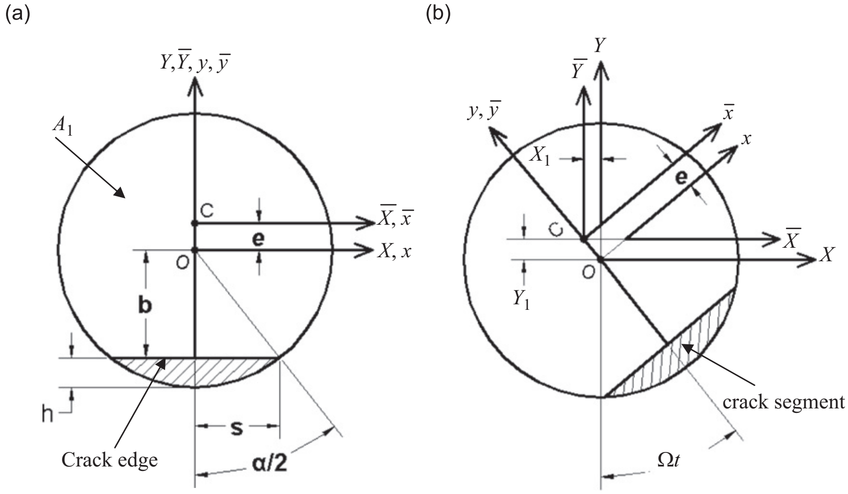

Fig. 2. Schematic diagrams of the cracked element cross-section: (a) before rotation and (b) after the shaft rotates. The dashed area represents the crack segment.

Table 1
Crack states for full angle of rotation (2π).

Rotation angle $0 \le \Omega t \le 2\pi$	States of the breathing crack
$0 \le \Omega t < \theta_1$, $2\pi - \theta_1 \le \Omega t < 2\pi$	Fully open
$\theta_1 \le \Omega t < (\pi+\alpha)/2$, $\pi - \alpha/2 \le \Omega t < 2\pi - \theta_1$	Partially open
$(\pi+\alpha)/2 \le \Omega t \le (3\pi - \alpha)/2$	Fully closed

where $\mu = h/R$ is the non-dimensional crack depth, h is the crack depth in the radial direction and $\gamma = \sqrt{\mu(2-\mu)}$. The crack states for a full rotation angle (2π) are shown in Table 1. The crack starts to close at $\Omega t = \theta_1$ at which the upper end of the crack edge reaches the compression stress field as shown in Fig. 1b. The crack becomes fully closed at $\Omega t = \theta_2$ as shown in Fig. 1f where $\theta_1$and θ_2 are given as

$$\theta_1 = \tan^{-1}\left(\frac{e + R(1-\mu)}{R\sqrt{\mu(2-\mu)}}\right), \quad \theta_2 = \frac{\pi}{2} + \cos^{-1}(1-\mu) \tag{2}$$

The cross-sectional area of the cracked element is equal to A_1 for $2\pi-\theta_1\leq\Omega t\leq\theta_1$. As the crack starts to close at $\Omega t=\theta_1$ the area of the closed portion of the crack is denoted by $A_2(t)$ which is a time-varying quantity. The overall cross-sectional area of the cracked element during rotation is then denoted by $A_{ce}(t)=A_1+A_2(t)$. The area moments of inertia of A_1 about the fixed X and Y axes for $t=0$ or about the rotated x and y axes for $t\geq 0$ are denoted by $I_1$and I_2, respectively. They are constant quantities that are calculated as

$$I_1=I-I_x^c \tag{3a}$$

$$I_2=I-I_y^c \tag{3b}$$

where $I=\pi R^4/4$ is the area moment of inertia of the shaft cross-section for the fully closed crack, R is the shaft radius, I_x^c and I_y^c are the area moments of inertia of the crack segment shown in Fig. 2 about the rotated x and y axes or the fixed X and Y axes, respectively. I_x^c and I_y^c are given as

$$I_x^c=\frac{\pi R^4}{8}-\frac{R^4}{4}((1-\mu)(2\mu^2-4\mu+1)\gamma+\sin^{-1}(1-\mu)) \tag{4a}$$

$$I_y^c=\frac{R^4}{12}((1-\mu)(2\mu^2-4\mu-3)\gamma+3\sin^{-1}(\gamma)) \tag{4b}$$

Here, we compare the above formulas of I_x^c and I_y^c with those found in Refs. [8–11] for a similar crack segment according the axes arrangement in Fig. 2 which are rewritten as

$$\tilde{I}_x=\frac{\pi R^4}{4}+R^4\left(\frac{2}{3}(1-\mu)\gamma^3+\frac{1}{4}(1-\mu)(1-4\mu+2\mu^2)\gamma+\sin^{-1}(\gamma)\right) \tag{5a}$$

$$\tilde{I}_y=\frac{R^4}{4}\left((1-\mu)(1-4\mu+2\mu^2)\gamma+\frac{\tilde{\alpha}}{2}\right) \tag{5b}$$

where $\tilde{\alpha}=2\cos^{-1}(1-\mu)$. In Table 2 we compare the results of the moments of inertia in Eq. (4), which are derived in this study, with $\tilde{I}_x$ and $\tilde{I}_y$ found in Refs. [8–11].

For $\mu=1$, the area moment of inertia about the X-axis should equal to that about the Y-axis as shown in Fig.3a since both of the cracked and the uncracked segments are semicircles which is not true for $\tilde{I}_x$ as shown in Table 2 and Fig. 3b. It is shown here that both $\tilde{I}_x$ and $\tilde{I}_y$ in Eq. (5) are inaccurate in calculating the area moments of inertia of a crack segment while the formulas for I_x^c and I_y^c in Eq. (4) derived in this study yield the accurate results.

Table 2
Area moments of inertia for $\mu=0$ and 1.

Crack depth	I_x^c	I_y^c	$\tilde{I}_x$	$\tilde{I}_y$
$\mu=0$	0	0	$\pi R^4/4$ or I?	0
$\mu=1$	$\pi R^4/8$	$\pi R^4/8$	$3\pi R^4/4$ or $3I$?	$\pi R^4/8$

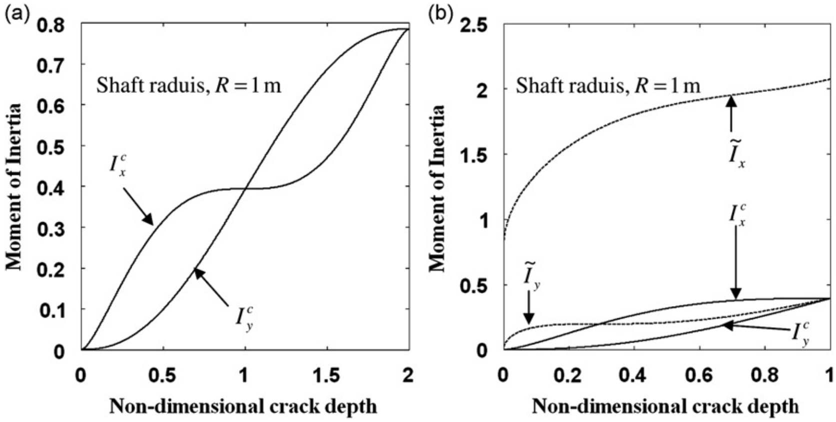

Fig. 3. (a) Area moments of inertia in (m^4) of the crack segment in the present study vs μ and (b) comparison between the area moments of inertia in the present study with the formulas found in Refs. [8–11].

The area moments of inertia of A_1 about the centroidal $\overline{X}$ and $\overline{Y}$ axes at $t=0$ or about the centroidal rotated $\bar{x}$ and $\bar{y}$ axes for $t \geq 0$ are given as

$$\bar{I}_1 = I_1 - A_1 e^2, \quad \bar{I}_2 = I_2 \tag{6}$$

The area moments of inertia of A_1 about the X and Y axes are time-varying quantities as the shaft rotates. They are calculated as [7]

$$I_X^{A_1}(t) = \frac{I_1+I_2}{2} + \frac{I_1-I_2}{2}\cos(2\Omega t) - I_{12}\sin(2\Omega t) \tag{7a}$$

$$I_Y^{A_1}(t) = \frac{I_1+I_2}{2} - \frac{I_1-I_2}{2}\cos(2\Omega t) + I_{12}\sin(2\Omega t) \tag{7b}$$

where Ω is the rotational speed of the shaft. Since y is the axis of symmetry of the cracked element cross-section during rotation, then $I_{12}=0$. The area moments of inertia of the area $A_2(t)$ about the X and Y axes which start to appear as the crack starts to close are denoted by $I_X^{A_2}(t)$ and $I_Y^{A_2}(t)$. For each time step, after the crack starts to close, the new values of the area $A_{\text{ce}}(t)$ and its area moments of inertia $I_X(t)$ and $I_Y(t)$ are calculated and the centroid location of $A_{\text{ce}}(t)$ is updated.

The orbits of the centroid of the overall cross-sectional area $A_{\text{ce}}(t)$ of the cracked element are plotted in Fig. 4a for different values of μ. In addition, $A_{\text{ce}}(t)$ is plotted in Fig. 4b for different values of μ.

The area moments of inertia of $A_{\text{ce}}(t)$ about the X and Y axes are calculated as

$$I_X(t) = I_X^{A_1}(t) + I_X^{A_2}(t) \tag{8a}$$

$$I_Y(t) = I_Y^{A_1}(t) + I_Y^{A_2}(t) \tag{8b}$$

Hence, the area moments of inertia of $A_{\text{ce}}(t)$ about the centroidal $\overline{X}$ and $\overline{Y}$ axes that stay parallel to the fixed X and Y axes during rotation are given as

$$I_{\overline{X}}(t) = I_X(t) - Y_{\text{ce}}(t)^2 A_{\text{ce}}(t) \tag{9a}$$

$$I_{\overline{Y}}(t) = I_Y(t) - X_{\text{ce}}(t)^2 A_{\text{ce}}(t) \tag{9b}$$

where $X_{\text{ce}}(t)$ and $Y_{\text{ce}}(t)$ are the centroid coordinates of $A_{\text{ce}}(t)$ relative to the fixed X and Y axes. The results of Eq. (9) are plotted in Fig. 5a for $I_{\overline{X}}(t)$ and in Fig. 5b for $I_{\overline{Y}}(t)$ for different values of μ. It is clear that the plot of $I_{\overline{X}}(t)$ is not similar to that of $I_{\overline{Y}}(t)$. Hence, each of these area moments of inertia follows a different breathing function during rotation.

Fig. 6 shows that $I_{\overline{X}}(t)+I_{\overline{Y}}(t)$ has nearly the same behavior of $A_{\text{ce}}(t)$ due to the crack breathing mechanism while neither $I_{\overline{X}}$ nor $I_{\overline{Y}}$ have similar behavior as shown before in Fig. 5.

An accurate functional relationship for $I_{\overline{X}}(t)$ is given as

$$I_{\overline{X}} \cong \hat{I}_{\overline{X}}(t) = I - (I - \bar{I}_1) f_1(t) \tag{10a}$$

$$f_1(t) = \left(\cos\left(\frac{1}{2}\Omega t\right)\right)^m = \frac{1}{2^m}\left(\binom{m}{m/2} + 2\sum_{j=0}^{(m/2)-1}\binom{m}{j}\cos\left((m-2j)\frac{\Omega}{2}t\right)\right) \tag{10b}$$

where I is the area moment of inertia when the crack is fully closed, $\bar{I}_1$ is given in Eq. (6) and m is a positive even number. Fig. 7 shows the high accuracy of the new formula of $\hat{I}_{\overline{X}}(t)$ given in Eq. (10) to approximate $I_{\overline{X}}(t)$.

To derive a formula for $I_{\overline{Y}}(t)$, it is simpler to introduce a formula for $I_{\overline{X}}(t)+I_{\overline{Y}}(t)$ than finding the Fourier series expansion of $I_{\overline{Y}}(t)$ itself since the formula for approximating $I_{\overline{X}}(t)$ is already introduced here. The Fourier series expansion gives an

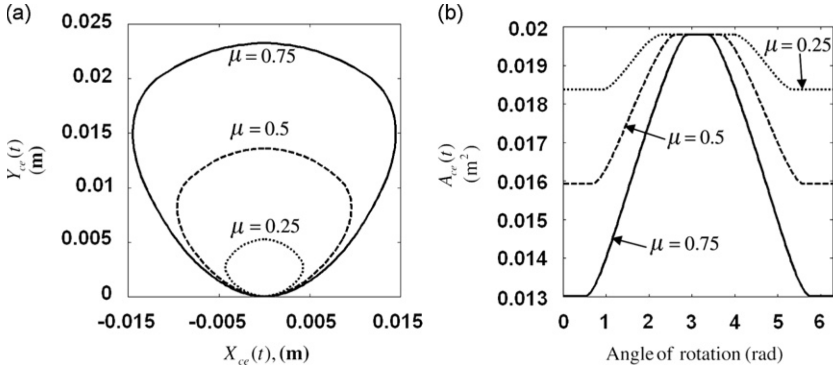

Fig. 4. (a) The orbits of the centroid of the overall cross-sectional area $A_{\text{ce}}(t)$ of the cracked element, (b) the overall cross-sectional area $A_{\text{ce}}(t)$ of the cracked element. The shaft radius is R=7.94 mm.

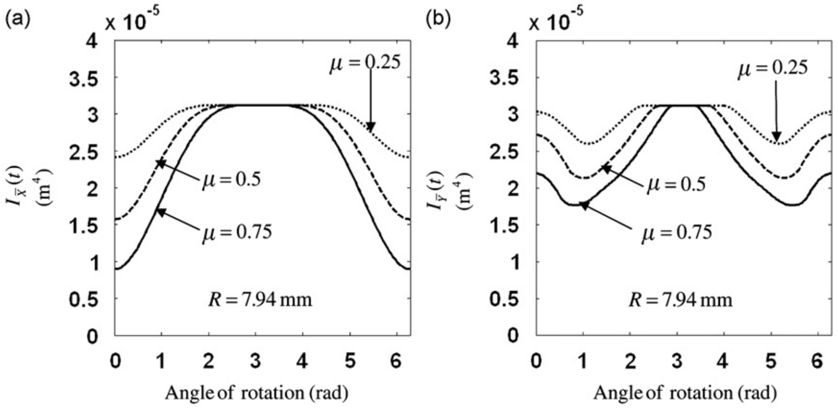

Fig. 5. Area moments of inertia of the cracked element cross-sectional area $A_{ce}(t)$ about the: (a) $\overline{X}$-axis and (b) $\overline{Y}$-axis.

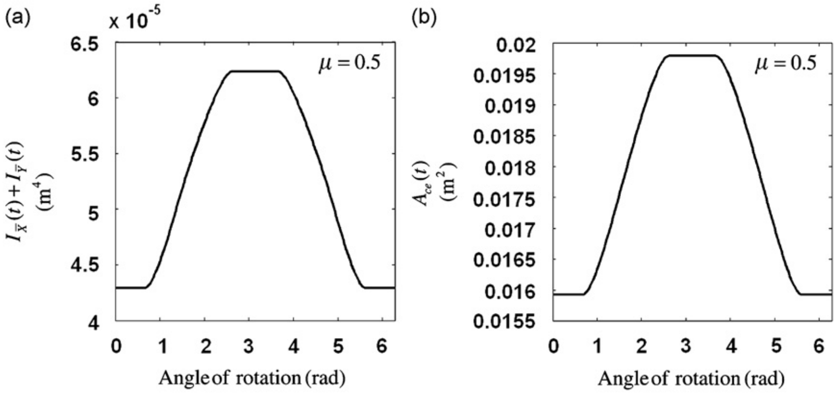

Fig. 6. (a) The sum of the area moments of inertia $I_{\overline{X}}(t)+I_{\overline{Y}}(t)$ of the cracked element cross-sectional area and (b) the cross-sectional area of the cracked element $A_{ce}(t)$. R=7.94 mm.

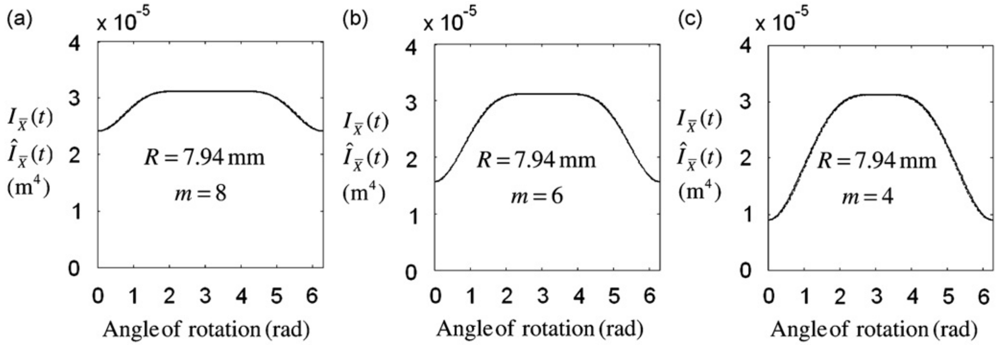

Fig. 7. Area moments of inertia about the $\overline{X}$-axis of the cracked element cross-sectional area. The solid lines represent $I_{\overline{X}}(t)$ and the dashed lines represent $\hat{I}_{\overline{X}}(t)$: (a) μ=0.25, (b) μ=0.5, and (c) μ=0.75.

approximate formula for $I_{\overline{X}}(t)+I_{\overline{Y}}(t)$ as

$$I_{\overline{X}}(t)+I_{\overline{Y}}(t) \cong \hat{I}_{\overline{X}}(t)+\hat{I}_{\overline{Y}}(t) = 2I-(2I-\overline{I}_1-\overline{I}_2)f_2(t) \tag{11a}$$

$$f_2(t)=\frac{1}{\pi}\left(-\frac{\theta_1+\theta_2}{2}+\frac{2}{(\theta_2-\theta_1)}\sum_{i=1}^{p}\frac{\cos(i\theta_2)-\cos(i\theta_1)}{i^2}\cos(i\Omega t)\right) \tag{11b}$$

Hence

$$I_{\overline{Y}}(t) \cong \hat{I}_{\overline{Y}}(t) = I + (I - \bar{I}_1) f_1(t) - (2I - \bar{I}_1 - \bar{I}_2) f_2(t) \tag{12}$$

Fig. 8 shows plots of the exact and approximate $I_{\overline{Y}}(t)$ and$I_{\overline{X}}(t)+I_{\overline{Y}}(t)$ using the formulas for $\hat{I}_{\overline{Y}}(t)$ and $\hat{I}_{\overline{X}}(t)+\hat{I}_{\overline{Y}}(t)$ in Eqs. (11) and (12) for i=4, m=8 and μ=0.3.

The approximate formulas for the area moments of inertia in Eqs. (10a) and (12) are rewritten as

$$\hat{I}_{\overline{X}}(t) = I - f_1(t) I_{11} \tag{13a}$$

$$\hat{I}_{\overline{Y}}(t) = I + f_1(t) I_{11} + I_{22} f_2(t) \tag{13b}$$

where $I_{11} = I - \bar{I}_1$, $I_{22} = -(2I - \bar{I}_1 - \bar{I}_2)$. Hence, the finite element stiffness matrix of the cracked element of the cracked rotor system is written as

$$\mathbf{k}_{ce}^{j} = \frac{E}{l^3} \begin{bmatrix} 12\hat{I}_{\overline{X}} & 0 & 0 & 6l\hat{I}_{\overline{X}} & -12l\hat{I}_{\overline{X}} & 0 & 0 & 6l\hat{I}_{\overline{X}} \\ 0 & 12\hat{I}_{\overline{Y}} & -6l\hat{I}_{\overline{Y}} & 0 & 0 & -12\hat{I}_{\overline{Y}} & -6l\hat{I}_{\overline{Y}} & 0 \\ 0 & -6l\hat{I}_{\overline{Y}} & 4l^2\hat{I}_{\overline{Y}} & 0 & 0 & 6l\hat{I}_{\overline{Y}} & 2l^2\hat{I}_{\overline{Y}} & 0 \\ 6l\hat{I}_{\overline{X}} & 0 & 0 & 4l^2\hat{I}_{\overline{X}} & -6l\hat{I}_{\overline{X}} & 0 & 0 & 2l^2\hat{I}_{\overline{X}} \\ -12l\hat{I}_{\overline{X}} & 0 & 0 & -6l\hat{I}_{\overline{X}} & 12\hat{I}_{\overline{X}} & 0 & 0 & -6l\hat{I}_{\overline{X}} \\ 0 & -12\hat{I}_{\overline{Y}} & 6l\hat{I}_{\overline{Y}} & 0 & 0 & 12\hat{I}_{\overline{Y}} & 6l\hat{I}_{\overline{Y}} & 0 \\ 0 & -6l\hat{I}_{\overline{Y}} & 2l^2\hat{I}_{\overline{Y}} & 0 & 0 & 6l\hat{I}_{\overline{Y}} & 4l^2\hat{I}_{\overline{Y}} & 0 \\ 6l\hat{I}_{\overline{X}} & 0 & 0 & 2l^2\hat{I}_{\overline{X}} & -6l\hat{I}_{\overline{X}} & 0 & 0 & 4l^2\hat{I}_{\overline{X}} \end{bmatrix} \tag{14}$$

Eq. (14) can be rewritten as

$$\mathbf{k}_{ce}^{j} = \mathbf{k}^{j} + \mathbf{k}_1^{j} f_1(t) + \mathbf{k}_2^{j} f_2(t) \tag{15}$$

where $\mathbf{k}^j$ is the stiffness matrix of cracked element j for fully closed crack state which is equivalent to the uncracked element stiffness matrix in Refs. [25,26]. The matrices $\mathbf{k}_1^j$ and $\mathbf{k}_2^j$ are the secondary stiffness matrices that appear due to the breathing crack. They are found via Eqs. (13) and (14) as

$$\mathbf{k}_1^{j} = \frac{E}{l^3} \begin{bmatrix} -12I_{11} & 0 & 0 & -6lI_{11} & 12lI_{11} & 0 & 0 & -6lI_{11} \\ 0 & 12I_{11} & -6lI_{11} & 0 & 0 & -12I_{11} & -6lI_{11} & 0 \\ 0 & -6lI_{11} & 4l^2I_{11} & 0 & 0 & 6lI_{11} & 2l^2I_{11} & 0 \\ -6lI_{11} & 0 & 0 & -4l^2I_{11} & 6lI_{11} & 0 & 0 & -2l^2I_{11} \\ 12lI_{11} & 0 & 0 & 6lI_{11} & -12I_{11} & 0 & 0 & 6lI_{11} \\ 0 & -12I_{11} & 6lI_{11} & 0 & 0 & 12I_{11} & 6lI_{11} & 0 \\ 0 & -6lI_{11} & 2l^2I_{11} & 0 & 0 & 6lI_{11} & 4l^2I_{11} & 0 \\ -6lI_{11} & 0 & 0 & -2l^2I_{11} & 6lI_{11} & 0 & 0 & -4l^2I_{11} \end{bmatrix} \tag{16a}$$

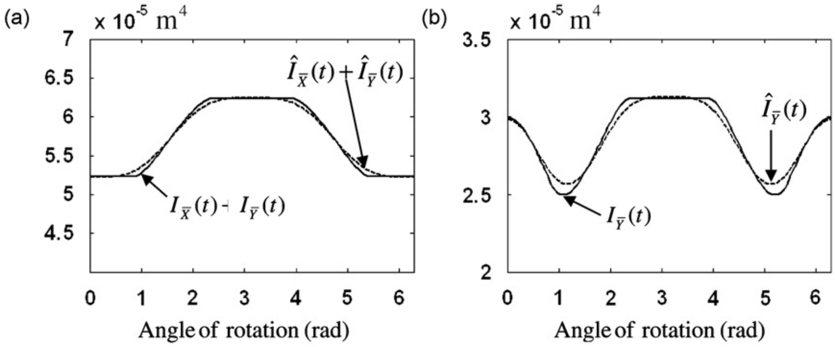

Fig. 8. (a) The exact and approximate $I_{\overline{X}}(t)+I_{\overline{Y}}(t)$ using $\hat{I}_{\overline{X}}(t)+\hat{I}_{\overline{Y}}(t)$ and (b) the exact and approximate $I_{\overline{Y}}(t)$ using $\hat{I}_{\overline{Y}}(t)$, p=4, m=8, μ=0.3 and R=7.94 mm.

$$\mathbf{k}_2^j=\frac{E}{l^3}\begin{bmatrix}0&0&0&0&0&0&0&0\\0&12I_{22}&-6lI_{22}&0&0&-12I_{22}&-6lI_{22}&0\\0&-6lI_{22}&4l^2I_{22}&0&0&6lI_{22}&2l^2I_{22}&0\\0&0&0&0&0&0&0&0\\0&0&0&0&0&0&0&0\\0&-12I_{22}&6lI_{22}&0&0&12I_{22}&6lI_{22}&0\\0&-6lI_{22}&2l^2I_{22}&0&0&6lI_{22}&4l^2I_{22}&0\\0&0&0&0&0&0&0&0\end{bmatrix} \tag{16b}$$

The FEM equations of motion of the cracked rotor-bearing-system with breathing crack model are written in matrix form as

$$\mathbf{M}\ddot{\mathbf{q}}(t)+\hat{\mathbf{C}}\dot{\mathbf{q}}(t)+(\mathbf{K}+\mathbf{K}_1f_1(t)+\mathbf{K}_2f_2(t))\mathbf{q}(t)=\mathbf{F}_1\cos\Omega t+\mathbf{F}_2\sin\Omega t+\mathbf{F}_g \tag{17}$$

where $\mathbf{q}(t)=[\mathbf{q}_1^{\mathrm{T}}\ldots\mathbf{q}_2^{\mathrm{T}}\ldots\mathbf{q}_i^{\mathrm{T}}\ldots\mathbf{q}_{N+1}^{\mathrm{T}}]^{\mathrm{T}}$ is the $4(N+1)\times 1$ dimension nodal displacement vector, $\mathbf{q}_i^{\mathrm{T}}(t)=[u_i\ v_i\ \phi_i^x\ \phi_i^y]$ is the single node displacement vector consisting of translational and rotational displacements about the X and Y axes for i=1,2, …, N+1, M is the global mass matrix, K is the global stiffness matrix of the uncracked system, $\mathbf{K}_1$ and $\mathbf{K}_2$ are the secondary stiffness matrices of zero entries except for the cracked element where the entries equal to $\mathbf{k}_1^j$ in $\mathbf{K}_1$ and equal to $\mathbf{k}_2^j$ in $\mathbf{K}_2$, $\hat{\mathbf{C}}=\mathbf{G}+\mathbf{C}$ is the global gyroscopic and damping matrix, F_1 and F_2 are $4(N+1)\times 1$ unbalance force amplitudes [12] and F_g is $4(N+1)\times 1$ gravity force vector. The single element mass, stiffness and gyroscopic matrices are found in Refs. [25,26]. The matrices $\mathbf{M}$, $\mathbf{K}$, $\mathbf{K}_1$, $\mathbf{K}_2$ and $\hat{\mathbf{C}}$ are each of dimension $4(N+1)\times 4(N+1)$. The functions $f_1(t)$ and $f_2(t)$ in Eqs. (10)–(12) and (17) can be expressed as

$$f_1(t)=a_o+\sum_{j=1}^{m}a_j\cos(j\Omega t),\quad f_2(t)=b_o+\sum_{j=1}^{p}b_j\cos(j\Omega t) \tag{18}$$

where p=2n and n is the number of harmonics used in the finite Fourier series solution

$$\mathbf{q}(t)=\mathbf{A}_0+\sum_{k=1}^{n}(\mathbf{A}_k\cos(k\Omega t)+\mathbf{B}_k\sin(k\Omega t)) \tag{19}$$

Inserting this solution in Eq. (17) yields

$$\begin{bmatrix}\tilde{\mathbf{C}} & 0.5\mathbf{C}_2^{(1)} & \mathbf{O} & 0.5\mathbf{C}_2^{(2)} & \mathbf{O} & 0.5\mathbf{C}_2^{(3)} & \mathbf{O} & 0.5\mathbf{C}_2^{(4)} & \cdots & \mathbf{O}\\ \mathbf{C}_2^{(1)} & \mathbf{C}^{(1)} & \mathbf{C}_1^{(1)} & \mathbf{C}_3^{(1,1)} & \mathbf{O} & \mathbf{C}_3^{(1,2)} & \mathbf{O} & \mathbf{C}_3^{(1,3)} & \cdots & \mathbf{O}\\ \mathbf{O} & -\mathbf{C}_1^{(1)} & \mathbf{C}^{(2)} & \mathbf{O} & \mathbf{C}_3^{(2,1)} & \mathbf{O} & \mathbf{C}_3^{(2,2)} & \mathbf{O} & \ddots & \mathbf{C}_3^{(2,n-1)}\\ \mathbf{C}_2^{(2)} & \mathbf{C}_3^{(1,1)} & \mathbf{O} & \mathbf{C}^{(3)} & \mathbf{C}_1^{(2)} & \mathbf{C}_3^{(3,1)} & \mathbf{O} & \mathbf{C}_3^{(3,2)} & \ddots & \mathbf{O}\\ \mathbf{O} & \mathbf{O} & \mathbf{C}_3^{(2,1)} & -\mathbf{C}_1^{(2)} & \mathbf{C}^{(4)} & \mathbf{O} & \mathbf{C}_3^{(4,1)} & \mathbf{O} & \ddots & \mathbf{C}_3^{(4,n-2)}\\ \mathbf{C}_2^{(3)} & \mathbf{C}_3^{(1,2)} & \mathbf{O} & \mathbf{C}_3^{(3,1)} & \mathbf{O} & \mathbf{C}^{(5)} & \mathbf{C}_1^{(3)} & \mathbf{C}_3^{(5,1)} & \ddots & \mathbf{O}\\ \mathbf{O} & \mathbf{O} & \mathbf{C}_3^{(2,2)} & \mathbf{O} & \mathbf{C}_3^{(4,1)} & -\mathbf{C}_1^{(3)} & \mathbf{C}^{(6)} & \mathbf{O} & \ddots & \vdots\\ \mathbf{C}_2^{(4)} & \mathbf{C}_3^{(1,3)} & \mathbf{O} & \mathbf{C}_3^{(3,2)} & \mathbf{O} & \mathbf{C}_3^{(5,1)} & \mathbf{O} & \ddots & \ddots & \mathbf{C}_3^{(2n-2,1)}\\ \vdots & \vdots & \ddots & \ddots & \ddots & \ddots & \ddots & \ddots & \mathbf{C}^{(2n-1)} & \mathbf{C}_1^{(n)}\\ \mathbf{O} & \mathbf{O} & \mathbf{C}_3^{(2,n-1)} & \mathbf{O} & \mathbf{C}_3^{(4,n-2)} & \mathbf{O} & \cdots & \mathbf{C}_3^{(2n-2,1)} & -\mathbf{C}_1^{(n)} & \mathbf{C}^{(2n)}\end{bmatrix}\begin{bmatrix}\mathbf{A}_o\\ \mathbf{A}_1\\ \mathbf{B}_1\\ \mathbf{A}_2\\ \mathbf{B}_2\\ \vdots\\ \mathbf{A}_{n-1}\\ \mathbf{B}_{n-1}\\ \mathbf{A}_n\\ \mathbf{B}_n\end{bmatrix}=\begin{bmatrix}\mathbf{F}_g\\ \mathbf{F}_1\\ \mathbf{F}_2\\ \mathbf{0}\\ \mathbf{0}\\ \mathbf{0}\\ \mathbf{0}\\ \mathbf{0}\\ \vdots\\ \mathbf{0}\end{bmatrix} \tag{20}$$

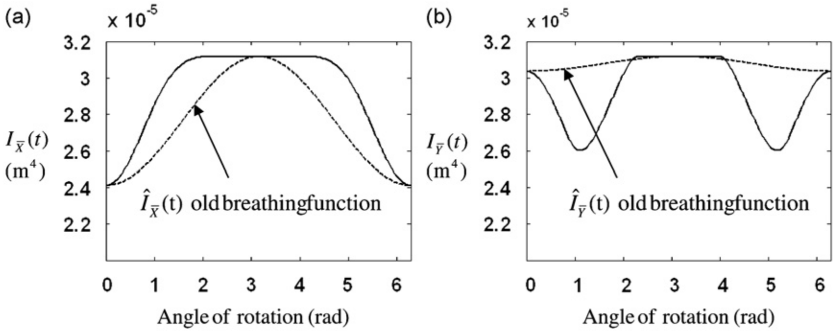

Fig. 9. The area moments of inertia (a) about $\bar{X}$-axis and (b) about $\bar{Y}$-axis of the cracked element cross-sectional area. The crack is assumed to be fully open at t=0. R=7.94 mm.

where $\tilde{\mathbf{C}}=\mathbf{K}+a_o\mathbf{K}_1+b_o\mathbf{K}_2$, $\mathbf{C}^{(i)}=\tilde{\mathbf{K}}-((i+1)\Omega/2)^2\mathbf{M}+(1/2)(a_{i+1}\mathbf{K}_1+b_{i+1}\mathbf{K}_2)$ for odd values of i (i=1,3,5, …, $2n-1$), $\mathbf{C}^{(i)}=\tilde{\mathbf{K}}-(i\Omega/2)^2\mathbf{M}-(1/2)(a_i\mathbf{K}_1+b_i\mathbf{K}_2)$ for even values of i (i=2,4,6, …, $2n$), $\mathbf{C}_1^{(i)}=i\Omega\hat{\mathbf{C}}$ for (i=1,2, …, n), $\mathbf{C}_2^{(i)}=a_i\mathbf{K}_1+b_i\mathbf{K}_2$ for (i=1,2, …, n) and $\mathbf{C}_3^{(k,i)}=(1/2)((a_{i+k+1}+a_i)\mathbf{K}_1+(b_{i+k+1}+b_i)\mathbf{K}_2)$ for odd values of k (k=1,3,5, …, $2n-3$), $\mathbf{C}_3^{(k,i)}=(1/2)((a_i-a_{i+k})\mathbf{K}_1+(b_i-b_{i+k})\mathbf{K}_2)$ for even values of k (k=2,4,6, …, $2n-2$) and O is of $4(N+1)\times 4(N+1)$ dimension matrix of zero entries.

3. Comparison with previous model for breathing mechanism

The classical form of the breathing crack function proposed in Ref. [13] and used in Refs. [8–12,23] to describe the breathing mechanism of the crack in a cracked rotor system is given by

$$f(t)=\frac{1}{2}(1\pm\cos(\Omega t)) \tag{21}$$

The plus sign of the cosine term in this function is used when the crack is fully open and symmetric with the negative Y-axis at t=0 while the negative sign is used when the crack is fully closed and symmetric with the positive Y-axis at t=0. The sign change of the cosine term only rotates the whirl orbit by 180° without affecting its shape. This function can be used in Eqs. (10a) and (12) by assuming $f_1(t)$=$f_2(t)$=$f(t)$ which yields

$$I_{\overline{X}}\cong\hat{I}_{\overline{X}}(t)=I-(I-\bar{I}_1)f(t) \tag{22a}$$

$$I_{\overline{X}}\cong\hat{I}_{\overline{X}}(t)=I-(I-\bar{I}_2)f(t) \tag{22b}$$

Eqs. (22a) and (22b) are exactly the same as the equations derived for the area moments of inertia for the cracked element of a similar cracked rotor system with a breathing crack in Ref. [12]. Hence, using the old breathing function in the literature given in Eq. (21) for approximating the breathing mechanism of a cracked rotor is a special case of our approach of using the more accurate breathing functions that given in Eq. (10). Fig. 9 shows the exact plots of $I_{\overline{X}}(t)$ and $I_{\overline{Y}}(t)$ and the plots of their approximate formulas using the old breathing function in Eq. (21). The figure shows the significant difference between the exact and the approximated formulas of these area moments of inertia. In the following section the results of using the old breathing function $f(t)$ and the new breathing functions $f_1(t)$ and $f_2(t)$ introduced here are compared for accuracy and validity for the rotor system with a breathing crack.

4. Theoretical results and analysis

The same finite element model used in Ref. [12] is used here as shown in Figs. 10 and 11. The undamped rotor-bearing-disk system is divided into 18 elements where the unbalance mass m_e is attached either to the right or left disk as shown in Fig. 11 at distance d from the shaft centerline. The values of the physical parameters are given in Table 3.

It is found that 4–6 harmonics are sufficient for the HB solution and give nearly the same shapes of orbits for a wide range of the rotor speeds in the neighborhood of the critical and subcritical speeds. In Fig. 12 the old breathing in Eq. (21) is compared with the new breathing functions proposed in this paper. It is shown that the old breathing function is not accurate in predicting the orbit shapes in the neighborhood of the subcritical speeds.

The results in Figs. 13 and14 were generated using 4 harmonics in the HB solution for $m_ed=1\times10^{-6}$ kg m. The waterfall plot in Fig. 13a shows the shift in the first pair of critical speeds versusμwhile the waterfall plot in Fig. 14a show the shift in the first pair of the subcritical speeds (∼1/2 of the first pair of the forward and backward whirling speeds). Each critical and subcritical speed is normalized to its corresponding value at $\mu\rightarrow 0$ for finding the percent shift in Figs. 13b and b as the

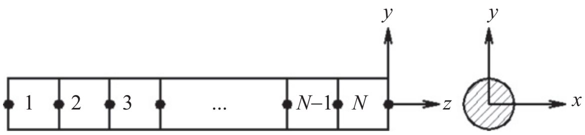

Fig. 10. Finite element model of the rotor.

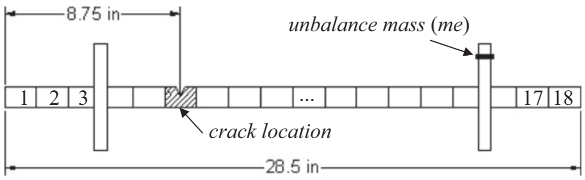

Fig. 11. Finite element model of rotor-disk-bearing system. There are 18 elements and the crack location is at element 6.

Table 3
Physical parameters of the MFS-RDS rotordynamic simulator.

Description	*Value*	*Description*	*Value*
Length of the rotor, L	0.724 m	Disk outer radius, R_o	0.0762 m
Radius of the rotor, R	1.588 mm	Disk inner radius, R_i	15.88 mm
Density of rotor, ρ	7800 kg/m^3	Density of disk, ρ	2700 kg/m^3
Modulus of elasticity, E	2.1×10^{11} N/m^2	Mass of the disk, m_d	0.571 kg
Bearing stiffness, (k_{xx}, k_{yy})	7×10^{7} N/m	Mass unbalance, m_ed	10^{-6} kg m
Bearing damping, (c_{xx}, c_{yy})	5×10^{2} N.s/m	Mass unbalance angle, β	0 rad

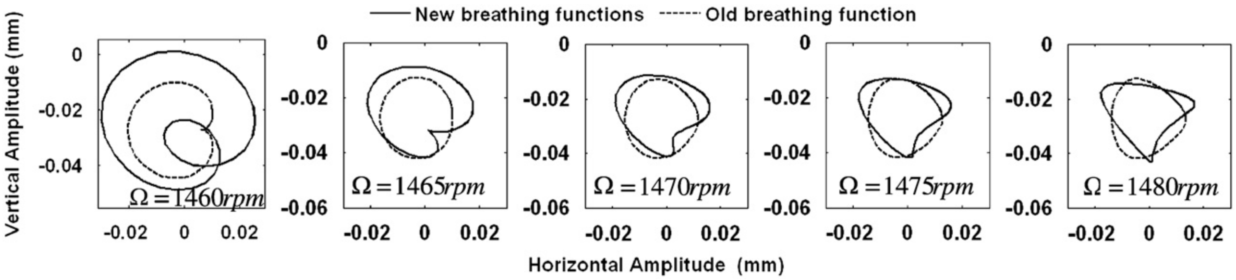

Fig. 12. Whirl orbits of node 1 of the cracked rotor system for different rotor speeds in the neighborhood of the first pair of the subcritical whirl speeds. $m_ed=4.5\times10^{-4}$ kg m, $\mu=0.3$.

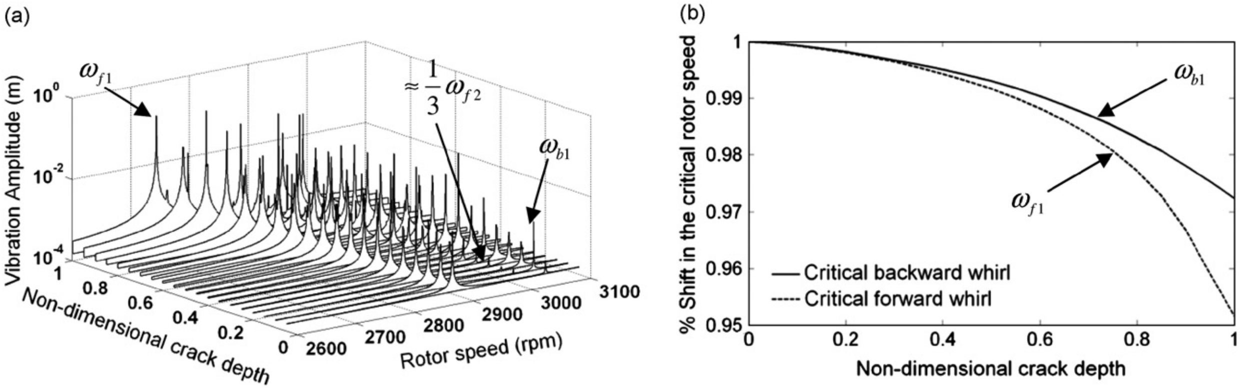

Fig. 13. (a) Waterfall plot showing the shift in the first critical forward and backward whirl speeds and (b) % shift in these critical whirl speeds versus μ. The amplitudes are calculated at node 10.

crack depth increases. The new peaks that start to appear at the critical and subcritical speeds can be tracked for the cracked system to detect the crack and its size. As the crack depth increases the shift in the critical and subcritical speeds increases which can give an approximation to the crack extent.

The peaks of the critical and subcritical speeds are plotted in Fig. 15. It is clear that while the cracked rotor passing through 1/2, 1/3 and 1/4 of the first pair of critical speeds, significant amplitudes of vibration appear for small crack depths. In addition, the subcritical speed that equivalent to nearly one third of the second critical forward whirl speed emerges peaks of vibration for small crack depth. These peaks, when tracked properly in real rotors, may give an early indication of crack propagation.

For $m_ed=3\times10^{-4}$ kg m and $\mu=0.3$ the first subcritical forward whirl occurs at rotor speed $\Omega=1456$ rpm while the first subcritical backward whirl occurs at rotor speed $\Omega=1495.5$ rpm. The orbits of the cracked rotor during the passage through these subcritical speeds are plotted in Fig. 16a–d for node 10 where the highest vibration amplitudes are expected to appear. The unbalance force is selected to maintain all vertical vibration amplitudes in this figure within the static deflection range of the cracked rotor. Similar to the observations in Ref. [20], the change in the stiffness is continues in the rotating-coordinate system which tends to generate higher frequency components in the response (i.e. 2 ×, 3 ×, … frequency components). The effect of the variation of the stiffness in the rotating-coordinate system appears clearly in Fig. 16. The whirl orbit plots before and after the subcritical forward whirl in Fig. 16a and b, respectively, agree with the

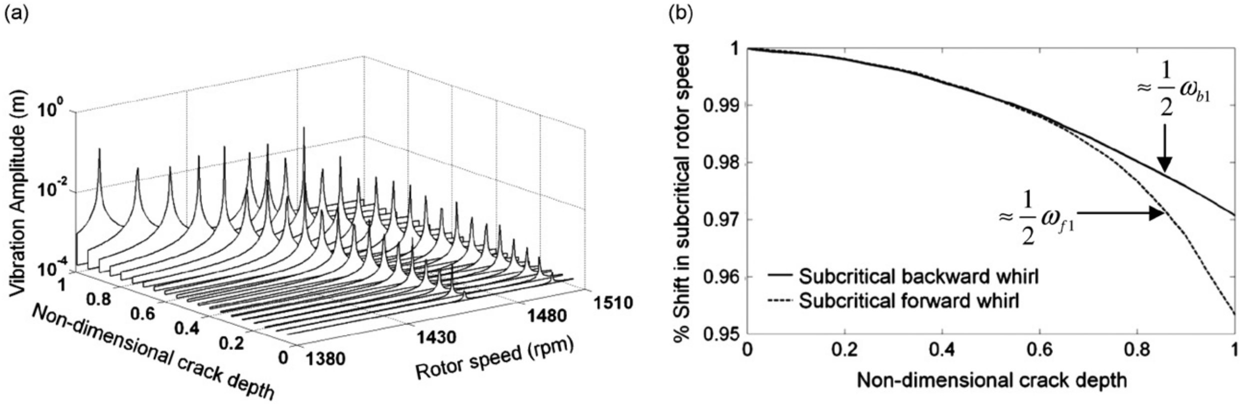

Fig. 14. (a) Waterfall plot showing the shift in the first subcritical forward and backward whirl speeds and (b) % shift in these subcritical whirl speeds versus μ. The amplitudes are calculated at node 10.

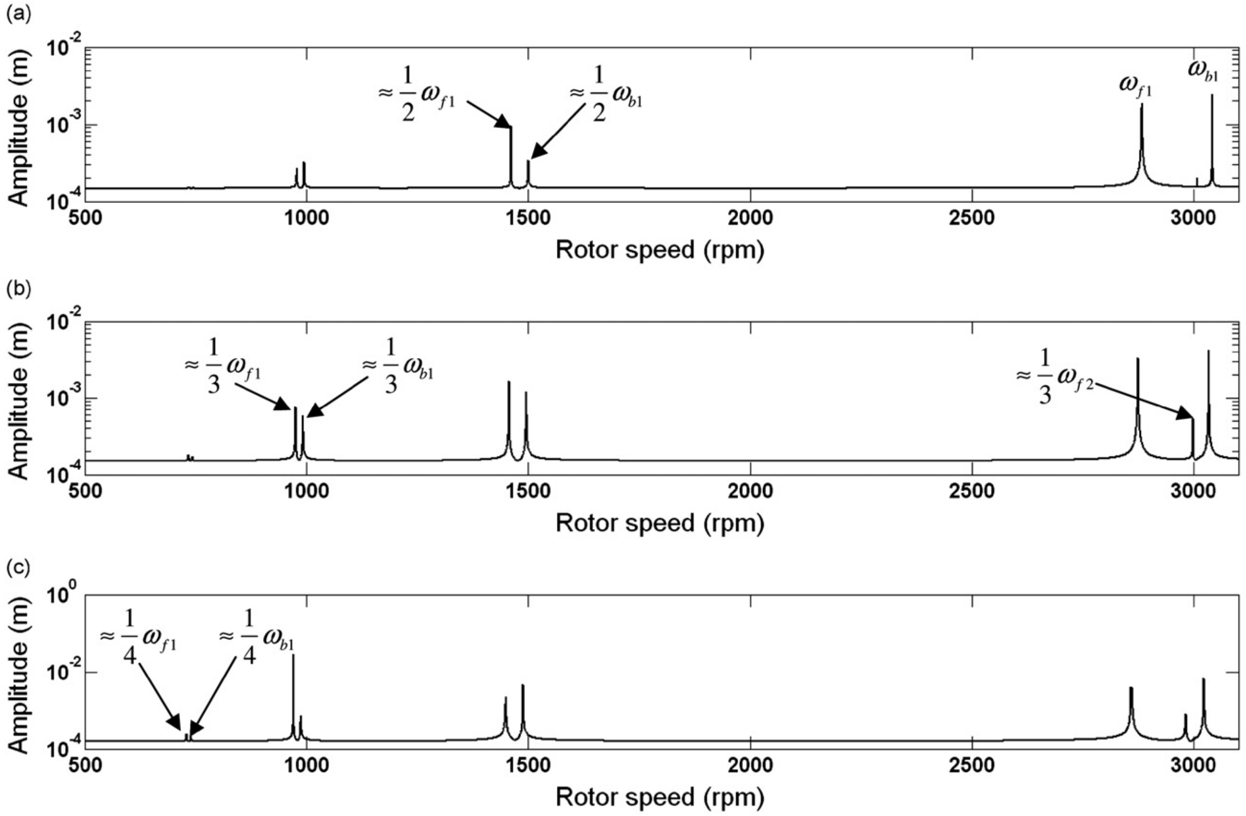

Fig. 15. Peaks of critical and subcritical speeds of the cracked rotor system for different values of μ: (a) μ=0.1, (b) μ=0.2, (c) μ=0.3. Amplitudes are calculated for node 10, $m_e d = 1 \times 10^{-6}$ kg m.

results in Refs. [15,18–21]. Similarly, the orbits of the cracked rotor during the passage through subcritical backward whirl are plotted in Fig. 16c and d, respectively, which agree with the results in Ref. [15]. Specifically, an excellent agreement is noticed about the whirl orbits during the passage through 1/2 and 1/3 of the critical speed between the results in Fig. 16 and the results in Ref. [20] where a cracked Jeffcott rotor with breathing crack was used. The orbit with one inner loop which is dominated by the 2× frequency component in Fig. 16a changes its direction by nearly $3\pi/4$ rad during the passage through 1/2 of the critical back whirl as shown in Fig. 16b. The similar theoretical orbit in Ref. [20] changes its direction by nearly πred and the similar experimental whirl orbit changes its direction by nearly $\pi/2$rad during the passage through 1/2 of the critical back whirl. The whirl orbit with two inner loops which is dominated by the 3× frequency

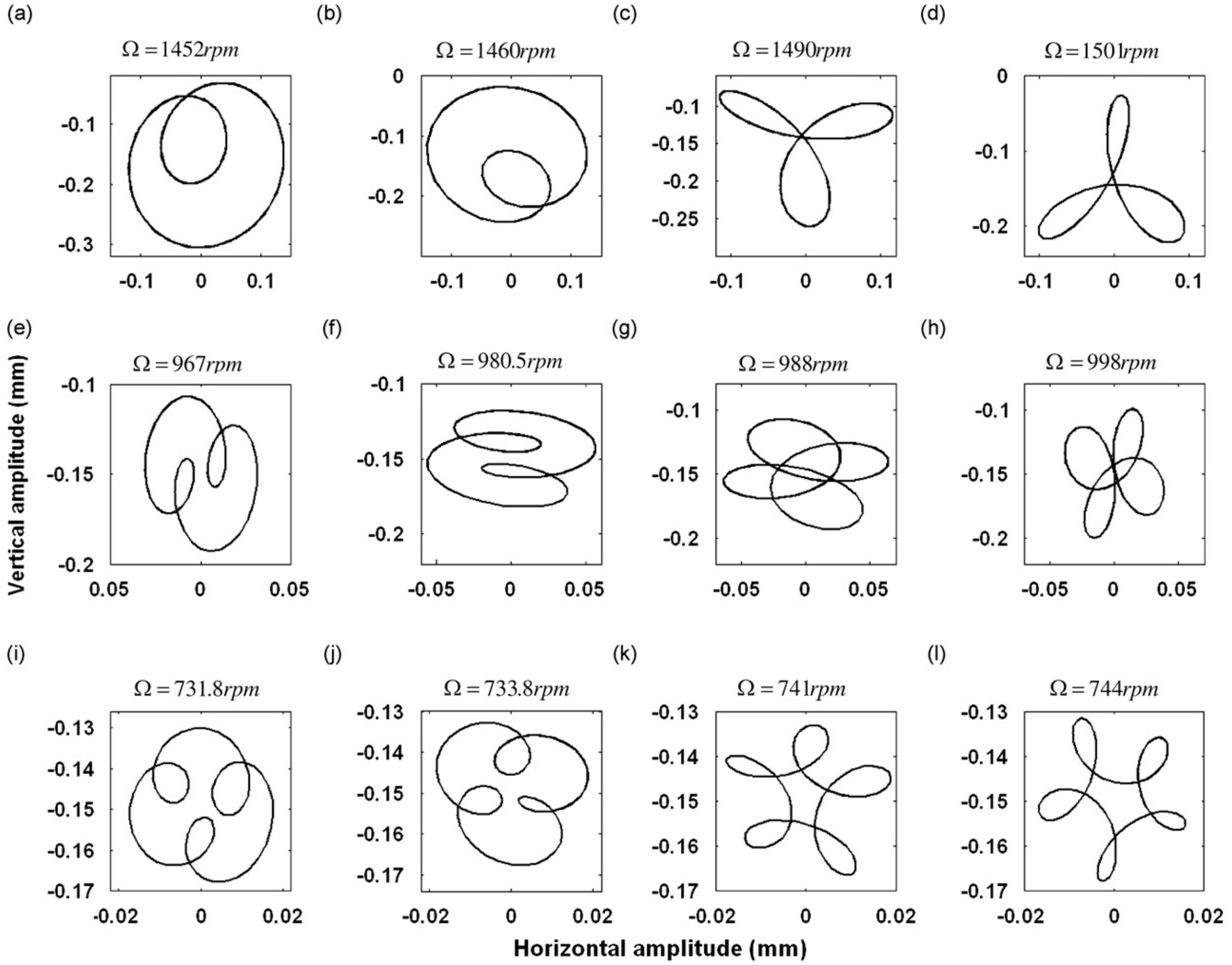

Fig. 16. Whirl orbits of node 10 of the cracked rotor system, (a)–(d) passage through 1/2 of the first pair of critical whirl speed, (e)–(h) passage through 1/3 of the first pair of critical whirl speeds, (i)–(l) passage through 1/4 of the first pair of critical whirl speeds $m_e d = 3\times 10^{-4}$ kg m, $\mu = 0.3$.

Table 4
Shapes of whirl orbits during the passage through subcritical speeds.

Subcritical speed	**Orbit shape**		**Response is dominated by**
	Passage through subcritical forward whirl	**Passage through subcritical backward whirl**	
1/2 first critical backward and forward whirl speeds	Orbit with one inner loop Fig. 16 (a and b)	Orbit with three outer loops Fig. 16 (c and d)	2 × harmonic component
1/3 first critical backward and forward whirl speeds	Orbit with two inner loops Fig. 16 (e and f)	Orbit with four outer loops Fig. 16 (g and h)	3 × harmonic component
1/4 first critical backward and forward whirl speeds	Orbit with three inner loops Fig. 16 (i and j)	Orbit with five outer loops Fig. 16 (k and l)	4 × harmonic component

component in Fig. 16e changes its direction by nearly $\pi/2$ rad during the passage through 1/3 of the critical forward whirl which agrees with the experimental observations about this whirl orbit in Ref. [20]. It is interesting that the behavior of the whirl orbits during the passage through the subcritical forward whirl is different from that at the subcritical backward whirl as shown in Fig. 16 and Table 4. The outer loops appear during the passage through the subcritical backward whirl while the inner loops appear during the passage through the subcritical forward whirl. Hence, we could distinguish between the subcritical backward whirl and forward whirl orbits through these inner and outer loops.

The difference between the whirl orbits during the passage through the subcritical backward whirl and the subcritical forward whirl speeds is the orientation and the number of the extra loops that appear in the orbit. This phenomenon can be utilized for crack detection in the cracked rotor.

The effect of unbalance phase angle β with the crack direction at $t=0$ is shown in Fig. 17 for $\Omega=1460$ rpm. For unbalance angle $\beta=0$ the crack opening is in the same direction of the unbalance mass location while for unbalance angle $\beta=\pi$ the crack opening is in the opposite direction of the unbalance mass location at $t=0$. The figure shows the sensitivity of the size and orientation of the orbit inner loop to the unbalance force location. This behavior, which agrees with the results in Ref. [21] for the cracked rotor, can be utilized as a way of crack detection.

The crack location is found affecting the whirl orbit only if it is close to the end of the shaft or to the bearings as shown in Fig. 18. The inner loop reverses its direction by nearly πrad when the crack occurs in element 18 which is close to the right bearing. In addition, the size of the inner loop is found to be much smaller than its size when the crack occurs away from the rotor ends. Hence, as the crack occurs away from the rotor center (i.e. close to the rotor ends) the behavior of the whirl orbit is different.

5. Experimental results

The similarity between the theoretical whirl orbits in the neighborhood of the subcritical whirl speeds in this study has an excellent agreement with those experimental orbits in Ref. [20]. However, the Spectra-Quest MFS-RDS rotordynamic simulator, shown in Fig. 19, was used here for finding the experimental whirl orbits for node 2 of the finite element model of the rotor system in the neighborhood of 1/2 of the first pair of the critical speeds. The physical parameters of the

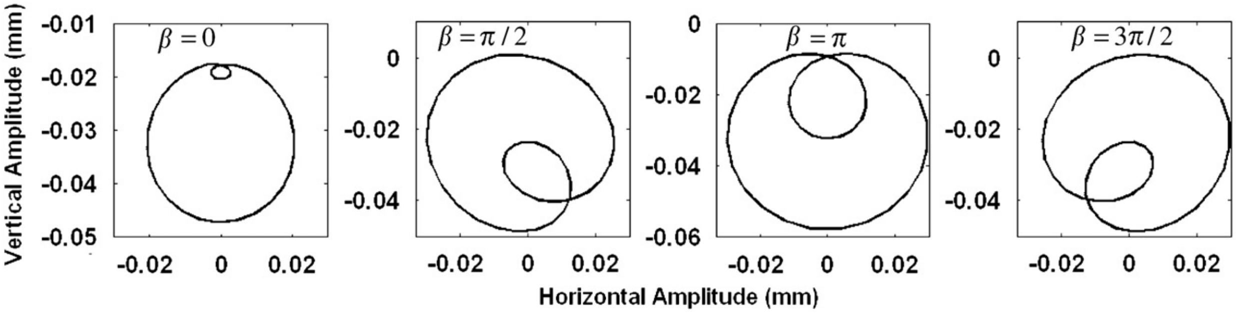

Fig. 17. Whirl orbits of node 1 of the cracked rotor system for different unbalance angles with positive X-axis: $m_ed=4.5\times10^{-4}$ kg m, $\mu=0.3$ and $\Omega=1460$ rpm.

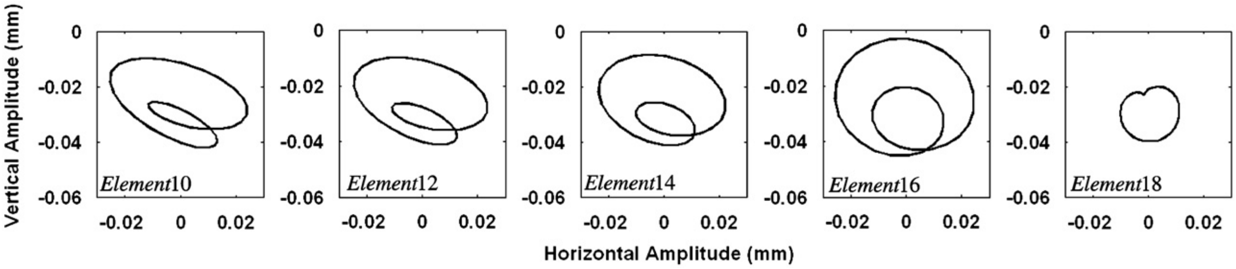

Fig. 18. Whirl orbits of node 1 of the cracked rotor system for different cracked element locations: $\mu=0.5$, $m_ed=3\times10^{-4}$ kg m, and $\Omega=1460$.

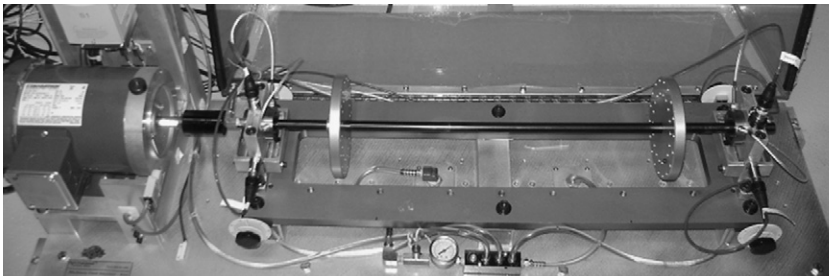

Fig. 19. MFS-RDS rotordynamic simulator used for experimental analysis.

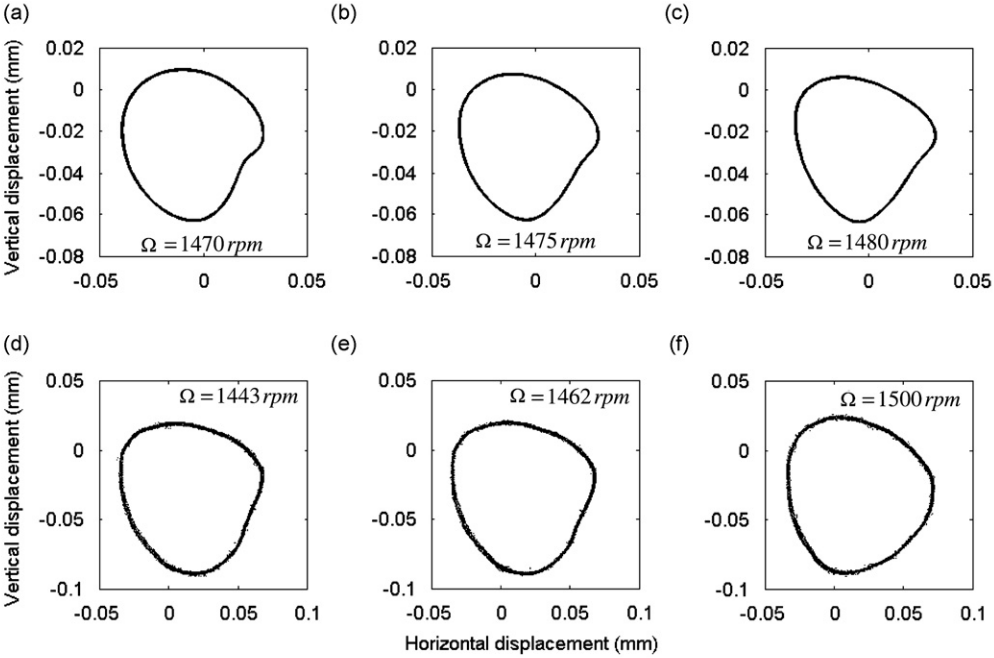

Fig. 20. Comparison of the theoretical and experimental orbits of the cracked rotor with breathing crack for μ=0.46, $m_e d$=6.3 × 10^{-4} kg m, (a)–(c) theoretical orbits, (d)–(f) experimental orbits.

MFS-RDS rotordynamic simulator have been previously given in Table 3. Two proximity probes have been installed close to node 2 for the horizontal and vertical displacements. The shaft has a built in breathing crack located in element 6 with μ=0.46. The experimental whirl orbits were found to be close to the theoretical orbits for some selected rotor speeds in the neighborhood of 1/2 of the critical rotational speed as shown in Fig. 20. The theoretical whirl orbit at Ω=1475 rpm in Fig. 20b is very close in shape and direction to the experimental whirl orbit in Fig. 20e for Ω=1462 rpm.

6. Conclusions

An efficient model for the correct breathing mechanism of the transverse breathing crack in a cracked rotor system is introduced in this study. The correct time-varying stiffness matrix of the cracked rotor depends on the time-varying area moments of inertia of the cracked element. Hence, two new breathing functions are introduced here and used in formulating the correct time-varying stiffness matrix of the cracked element. These new functions are considerably more accurate than the previously used one in Refs. [8–12,13]. The FEM equations of motion are then formulated and the time-varying stiffness matrix of the cracked element is incorporated into the global stiffness matrix of the system in the finite element model. The finite element model of the system was solved via the harmonic balance method for response, orbits, and critical and subcritical rotational speeds. In addition, the efficiency of this approach is shown by comparison with some recent published results in Refs. [15,18–21].

The efficient model of the breathing crack and the harmonic balance solution in this study for the cracked rotor system have resulted in significant observations. The exact critical and subcritical speeds and their shift due to the increase in the crack depth have been obtained from the waterfall plots. The shift in both critical and subcritical speeds may give an approximation to the crack depth. In addition, the well-known orbit with two loops is shown to appear during the passage through the first subcritical forward whirl while this was verified in the previous studies. The orbit with three outer loops appears during the passage through the first subcritical backward whirl. These orbits which appear within the static deflection range for relatively high unbalance force can be used for detecting the breathing crack at small crack depths. Hence, the appearance of the inner loops of the orbits during the passage through the subcritical forward whirl and of the outer loops during the passage through the subcritical backward whirl is a significant phenomenon for crack detection. These orbits are sensitive to the unbalance force direction which may also help in detecting the crack at the beginning of its growth. The crack location only affects the orbits in the neighborhood of the subcritical speeds when this location is very close to the bearings. The vibration amplitudes at the first and second pairs of the subcritical whirl speeds were found to be significant for crack detection even for small crack depths. In addition, our theoretical and experimental findings demonstrate good agreement while they also match well with well-known theoretical and experimental results in the literature.

Based on the approach of this study, different techniques can be utilized for detecting the crack in the rotor system at the same time. These include knowledge of the exact critical and subcritical whirl speeds, the shift in these critical and subcritical whirl speeds, whirl orbits with inner or outer loops in the neighborhood of the subcritical whirl speeds, the sensitivity of these whirl orbits to the location of unbalance force, and the significant vibration amplitudes at these subcritical speeds.

Acknowledgement

Financial support of NASA under Grant no. GR0002488 is gratefully acknowledged.

Appendix A. Calculation of the area, centroid and the area moments of inertia of the cracked and the uncracked segments of the cracked element cross-section

The cracked element cross-section is shown in Fig. A1a where A_c represents the area of the crack segment and A_1 represents the left uncracked area. The quantities b and s in Fig. A1b can be rewritten in term of the crack depth ratio $\mu=h/R$ as $b=R(1-\mu)$ and $s=R\gamma$ where $\gamma=\sqrt{\mu(2-\mu)}$. The area A_c of the crack segment is calculated as

$$\begin{aligned} A_c &= \int_{A_c} \mathrm{d}A_x = 2\int_0^s (y-b)\,\mathrm{d}x = 2\int_0^s (\sqrt{R^2-x^2}-b)\,\mathrm{d}x \\ &= R^2\sin^{-1}\left(\frac{s}{R}\right)+s\sqrt{R^2-s^2}-2bs \\ &= R^2\sin^{-1}\gamma-R^2(1-\mu)\gamma \end{aligned} \tag{A1}$$

For $\alpha/2=\sin^{-1}\gamma=\cos^{-1}(1-\mu)$ Eq. (A1) becomes

$$A_c = R^2\cos^{-1}(1-\mu)-R^2(1-\mu)\gamma \tag{A2}$$

Hence

$$A_1 = \pi R^2-A_c = R^2(\pi-\cos^{-1}(1-\mu)+(1-\mu)\gamma) \tag{A3}$$

The centroid location of the area A_1 on the Y-axis is calculated by integrating over the area as

$$\begin{aligned} e &= \frac{1}{A_1}\int_{-R}^{b} y(2x\,\mathrm{d}y) = \frac{2}{A_1}\int_{-R}^{b} y\sqrt{R^2-y^2}\,\mathrm{d}y = \frac{2}{3A_1}(R^2-b^2)^{3/2} \\ &= \frac{2R^3}{3A_1}\left(\mu(2-\mu)\right)^{3/2} = \frac{2R^3}{3A_1}\gamma^3 \end{aligned} \tag{A4}$$

The area moments of inertia of the crack segment about the fixed X and Y axes or the rotating x and y axes are derived, respectively, as

$$\begin{aligned} I_X^c = I_x^c &= \int_{A_c} y^2\,\mathrm{d}A_y = 2\int_b^R y^2 x\,\mathrm{d}y = 2\int_b^R y^2\sqrt{R^2-y^2}\,\mathrm{d}y \\ &= \frac{\pi R^4}{8}-\frac{1}{4}\left(R^4\sin^{-1}\left(\frac{b}{R}\right)-\sqrt{R^2-b^2}(bR^2-2b^3)\right) \end{aligned}$$

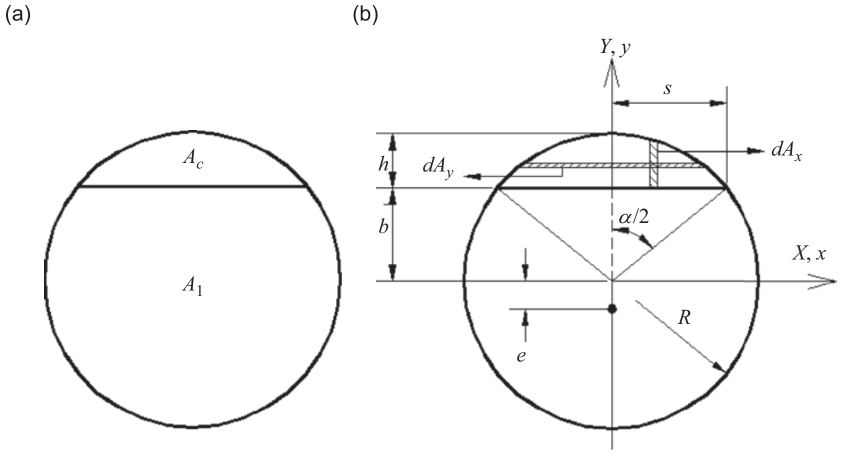

Fig. A1. (a) and (b) schematic diagrams of the cracked element cross-section.

$$
\begin{aligned}
&= \frac{\pi R^4}{8} - \frac{1}{4}\left(R^4 \sin^{-1}(1-\mu) - \sqrt{R^2-b^2}(bR^2-2b^3)\right) \\
&= \frac{\pi R^4}{8} - \frac{R^4}{4}((1-\mu)(2\mu^2-4\mu+1)\gamma + \sin^{-1}(1-\mu))
\end{aligned} \tag{A5}
$$

$$
\begin{aligned}
I_Y^c = I_y^c &= \int_{A_c} x^2\,\mathrm{d}A_x = 2\int_0^s x^2(y-b)\,\mathrm{d}x = 2\int_0^s x^2(\sqrt{R^2-x^2}-b)\,\mathrm{d}x \\
&= \frac{1}{12}\left(3R^4 \sin^{-1}\left(\frac{s}{R}\right) - \sqrt{R^2-s^2}(3sR^2-6s^3) - 8bs^3\right) \\
&= \frac{R^4}{12}((1-\mu)(2\mu^2-4\mu-3)\gamma + 3\sin^{-1}(\gamma))
\end{aligned} \tag{A6}
$$

Appendix B. Calculations of the area, centroid and the area moments of inertia of the cracked element cross-section

The closed portion of the crack is represented by the thick boundary in Fig. B1 where the area of this closed portion is $A_2 = A_3 + A_4$. As the upper corner of the crack reaches the compression stress field at $\theta = \theta_1$ the further increase in θ ($\theta > \theta_1$) makes the crack start to close forming the closed portion of area A_2 in which the areas A_3 and A_4 are formed. The initial guess for the new centroid location at the new angle $\theta > \theta_1$ is $Y_{ce}^{(1)} = e\cos(\theta_1)$ where the angles in Fig. B1 are calculated as

$$
\delta = \sin^{-1}\left(\frac{Y_{\mathrm{ce}}}{R}\right), \quad \beta = \left(\theta + \frac{\alpha}{2} - \delta - \frac{\pi}{2}\right), \quad \phi = \frac{\pi}{2} - (\beta+\delta), \quad \varphi = \frac{\pi}{2} - \frac{\alpha}{2}, \quad \rho = \phi - \varphi \tag{B1}
$$

The integration limits for calculating the areas, area moments of inertia and the centroids are given as

$$
\begin{aligned}
&a_1 = R\cos(\beta+\delta), \quad a_2 = R\cos(\delta), \quad b_1 = Y_{ce} \\
&b_2 = R\sin(\beta+\delta), \quad a_o = a_1 - (b_2-b_1)\tan(\rho)
\end{aligned} \tag{B2}
$$

The area A_3 and its centroidal coordinates relative to the fixed X and Y axes are calculated as

$$
A_3 = \int_{A_3} \mathrm{d}A_x = \int_{a_1}^{a_2} (y-b_1)\,\mathrm{d}x = \int_{a_1}^{a_2} \left(\sqrt{R^2-x^2} - b_1\right)\mathrm{d}x \tag{B3a}
$$

$$
X_3 = \frac{1}{A_3}\int_{a_1}^{a_2} x\,\mathrm{d}A_x = \frac{1}{A_3}\int_{a_1}^{a_2} x\left(\sqrt{R^2-x^2} - b_1\right)\mathrm{d}x \tag{B3b}
$$

$$
Y_3 = \frac{1}{A_3}\int_{b_1}^{b_2} y\,\mathrm{d}A_y = \frac{1}{A_3}\int_{b_1}^{b_2} y\left(\sqrt{R^2-y^2} - a_1\right)\mathrm{d}y \tag{B3c}
$$

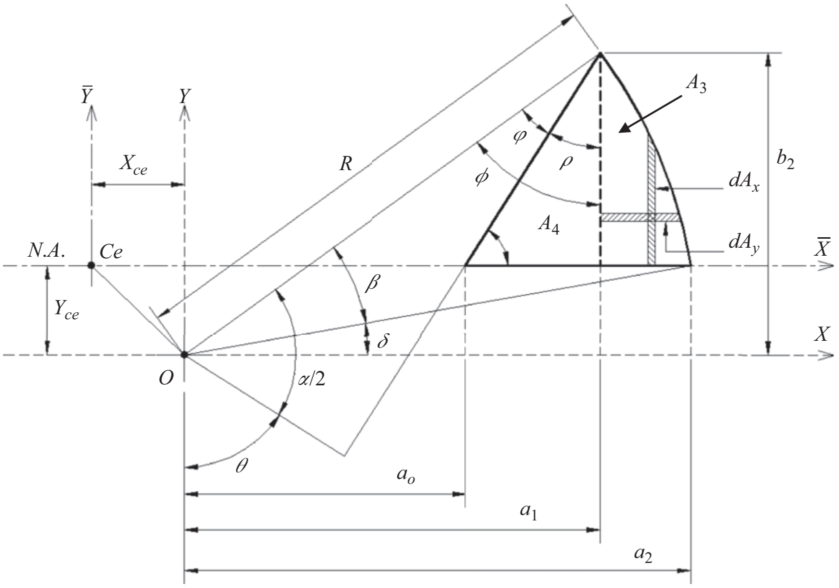

Fig. B1. Schematic diagram showing all necessary angles and quantities for calculating area, centroid and the area moments of inertia of the closed portion of the breathing crack.

Similarly, the area A_4 and its centroidal coordinates relative to the fixed X and Y axes are calculated as

$$A_4 = \frac{1}{2}(b_2 - b_1)(a_1 - a_o) \tag{B4a}$$

$$X_4 = a_o + \frac{(a_1 - a_o)}{3} \tag{B4b}$$

$$Y_4 = b_1 + \frac{(b_2 - b_1)}{3} \tag{B4c}$$

The cracked element cross-sectional area is $A_{\mathrm{ce}}=A_1+A_3+A_4$. The centroid coordinates of A_{ce} are calculated relative to the fixed X and Y axes as

$$\begin{aligned} X_{\mathrm{ce}} &= \frac{A_1X_1 + A_3X_3 + A_4X_4}{A_{\mathrm{ce}}} \\ Y_{\mathrm{ce}} &= \frac{A_1Y_1 + A_3Y_3 + A_4Y_4}{A_{\mathrm{ce}}} \end{aligned} \tag{B5}$$

where $X_1 = -e\cos\theta$ and $Y_1 = e\sin\theta$ are the centroid coordinates of A_1 in the fixed X and Y axes.

An iterative procedure on Y_{ce} is repeated as $Y_{\mathrm{ce}}^{(k+1)} = (Y_{\mathrm{ce}}^{(k)} + Y_{\mathrm{ce}}^{(k-1)})/2$ and Eqs. (B1)–(B5) are recalculated for each iteration step until $(Y_{\mathrm{ce}}^{(k+1)} - Y_{\mathrm{ce}}^{(k)}) \rightarrow 0(\mathit{minimum})$ where the exact centroid coordinates of the cracked element cross-sectional area are located. Once the exact location of the centroid is located, the integration limits a_1, a_2, b_1 and b_2 are recalculated where the area moments of inertia for A_3 and A_4 about the fixed X and Y axes are calculated as

$$\begin{aligned} I_X^{A_3} &= \int_{A_3} y^2\,\mathrm{d}A_y = \int_{b_1}^{b_2} y^2(x - a_1)\,\mathrm{d}y = \int_{b_1}^{b_2} y^2\left(\sqrt{R^2 - y^2} - a_1\right)\mathrm{d}y \\ I_Y^{A_3} &= \int_{A_3} x^2\,\mathrm{d}A_x = \int_{a_1}^{a_2} x^2(y - b_1)\,\mathrm{d}x = \int_{a_1}^{a_2} x^2\left(\sqrt{R^2 - x^2} - b_1\right)\mathrm{d}x \end{aligned} \tag{B6}$$

$$\begin{aligned} I_X^{A_4} &= \frac{1}{36}(a_1 - a_o)(b_2 - b_1)^3 + A_4(Y_4)^2 \\ I_Y^{A_4} &= \frac{1}{36}(b_2 - b_1)(a_1 - a_o)^3 + A_4(X_4)^2 \end{aligned} \tag{B7}$$

The area moments of inertia of A_1 in Appendix A and of A_3 and A_4 are calculated about the fixed X and Y axes. Hence, the overall area moments of inertia of the cracked element cross-sectional area A_{ce} at $\theta > \theta_1$are calculated as

$$\begin{aligned} I_X^{A_{\mathrm{ce}}} &= I_X = I_X^{A_1} + I_X^{A_3} + I_X^{A_4} \\ I_Y^{A_{\mathrm{ce}}} &= I_Y = I_Y^{A_1} + I_Y^{A_3} + I_Y^{A_4} \end{aligned} \tag{B8}$$

These area moments of inertia are recalculated about the centroid of A_{ce} (X_{ce}, Y_{ce}) as

$$\begin{aligned} I_{\overline{X}} &= I_X - A_{\mathrm{ce}}(Y_{\mathrm{ce}})^2 \\ I_{\overline{Y}} &= I_Y - A_{\mathrm{ce}}(X_{\mathrm{ce}})^2 \end{aligned} \tag{B9}$$

For each new angle of rotation all steps in Eqs. (B1)–(B9) are repeated until the crack becomes fully closed.

References

[1] C.A. Papadopoulos, A.D. Dimarogonas, Coupled longitudinal and vertical vibrations of a rotating shaft with an open crack, *Journal of Sound and Vibration* 117 (1) (1987) 81–93.

[2] A.C. Chasalevris, C.A. Papadopoulos, Coupled horizontal and vertical bending vibrations of stationary shaft with two cracks, *Journal of Sound and Vibration* 309 (2007) 507–528.

[3] A.S. Sekhar, B.S. Prabhu, Transient analysis of a cracked rotor passing through critical speeds, *Journal of Sound and Vibration* 173 (3) (1994) 415–421.

[4] A.S. Sekhar, Crack identification in a rotor system: a model-based approach, *Journal of Sound and Vibration* 270 (2004) 887–902.

[5] A.S. Sekhar, A.R. Monhanty, S. Prabhakar, Vibration of cracked rotor system: transverse crack versus slant crack, *Journal of Sound and Vibration* 279 (2005) 1203–1217.

[6] A.K. Darpe, A novel way to detect transverse surface crack in a rotating shaft, *Journal of Sound and Vibration* 305 (2007) 151–171.

[7] W.D. Pilkey, *Analysis and Design of Elastic Beams*, first ed., John Wiley & Sons, New York, 2002, pp. 24–29.

[8] J. Sinou, Detection of cracks in rotor based on the 2 × and 3 × super-harmonics frequency components and the crack-unbalance interactions, *Communications in Nonlinear Science and Numerical Simulation* 13 (2008) 2024–2040.

[9] J. Sinou, A.W. Lees, A non-linear study of a cracked rotor, *European Journal of Mechanics* 26 (2007) 152–170.

[10] J. Sinou, A.W. Lees, The influence of cracks in rotating shafts, *Journal of Sound and Vibration* 285 (2005) 1015–1037.

[11] J. Sinou, Effects of a crack on the stability of a non-linear rotor system, *International Journal of Non-Linear Mechanics* 42 (7) (2007) 959–972.

[12] M.A. Al-Shudeifat, E.A. Butcher, C.R. Stern, General harmonic balance solution of a cracked rotor-bearing-disk system for harmonic and sub-harmonic analysis: analytical and experimental approach, *International Journal of Engineering Science*, doi:10.1016/j.ijengsci.2010.05.012.

[13] I.W. Mayes, W.G.R. Davies, Analysis of the response of a multi-rotor-bearing system containing a transverse crack in a rotor, *Journal of Vibration, Acoustics, Stress, and Reliability in Design* 106 (1984) 139–145.

[14] I. Green, C. Casy, Crack detection in a rotor dynamic system by vibration monitoring—part I: analysis, *Journal of Engineering for Gas Turbine and Power* 127 (2005) 425–436.

[15] O.S. Jun, M.S. Gadala, Dynamic behavior analysis of cracked rotor, *Journal of Sound and Vibration* 309 (2008) 210–245.

[16] L. Xiao-feng, X. Ping-yong, S. Tie-lin, Y. Shu-zi, Nonlinear analysis of a cracked rotor with whirling, *Applied Mathematics and Mechanics* 23 (2002) 721–731.
[17] C.M. Stoisser, S. Audebert, A comprehensive theoretical, numerical and experimental approach for crack detection in power plant rotating machinery, *Mechanical Systems and Signal Processing* 22 (2008) 818–844.
[18] T.H. Patel, A.K. Darpe, Influence of crack breathing model on nonlinear dynamics of a cracked rotor, *Journal of Sound and Vibration* 311 (2008) 953–972.
[19] T. Zhou, Z. Sun, J. Xu, W. Han, Experimental analysis of a cracked rotor, *Journal of Dynamic Systems, Measurements, and Control* 127 (2005) 313–320.
[20] A.K. Darpe, K. Gupta, A. Chawla, Transient response and breathing behavior of a cracked Jeffcott rotor, *Journal of Sound and Vibration* 272 (2004) 207–243.
[21] A.K. Darpe, K. Gupta, A. Chawla, Dynamics of bowed rotor with transient surface crack, *Journal of Sound and Vibration* 296 (2006) 888–907.
[22] C.A. Papadopoulos, The strain energy release approach for modeling cracks in rotors: a state of the art review, *Mechanical Systems and Signal Processing* 22 (2008) 763–789.
[23] G. Litak, J.T. Sawicki, Intermittent behavior of a cracked rotor in the resonance region, *Chaos, Solitons & Fractals* 42 (3) (2009) 1495–1501.
[24] N. Bachschmid, P. Pennacchi, E. Tanzi, Some remarks on breathing mechanism, on non-linear effects and on slant and helicoidal cracks, *Mechanical Systems and Signal Processing* 22 (4) (2008) 879–904.
[25] M. Lalanne, G. Ferraris, *Rotor Dynamics Prediction in Engineering*, second ed., John Wiley & Sons, New York, 1998.
[26] T. Yamamoto, Y. Ishida, *Linear and Nonlinear Rotordynamics*, second ed., John Wiley & Sons, New York, 2001.